Enhancing Hyrcanian Forest Height and Aboveground Biomass Predictions: A Synergistic Use of TanDEM-X InSAR Coherence, Sentinel-1, and Sentinel-2 Data

Ghasem Ronoud, Ali A. Darvishsefat, Maryam Poorazimy, Erkki Tomppo, Oleg Antropov, *Member, IEEE*, and Jaan Praks, *Member, IEEE*

***Abstract*—Forest height (FH) is an important driver for aboveground biomass (AGB) that can be obtained using interferometric synthetic aperture radar (InSAR). However, the limited access to the quad-polarimetric data or high-accuracy terrain model makes FH retrieval a challenging task. This study aimed to retrieve FH and further predict AGB by combining TanDEM-X InSAR coherence, Sentinel-1 (S-1), and Sentinel-2 (S-2) data. A total of 125 sample plots with a size of 900 m^2 were established in a broadleaved forest of Kheyroud, Iran. The linear and sinc models obtained by simplification of the random volume over ground model were used for deriving $\mathrm{FH_{Lin}}$ and $\mathrm{FH_{Sinc}}$. Further investigation was conducted when S-1 and S-2 features including backscatters and multispectral information were added to FH predictions. Using the above-mentioned datasets and FH as an additional predictor, AGB was also predicted. *K*-nearest neighbor (*k*-NN), random forest (RF), and support vector regression (SVR) were employed for prediction. Lorey's mean height and AGB at sample plots were used in the accuracy assessment. Using the SVR method and synergy of $\mathrm{FH_{Sinc}}$, S-1, and S-2 features, the FH prediction was improved ($\mathrm{FH_{imp}}$) with RMSE of 3.18 m and $R^2 = 0.59$. The AGB prediction with RF and the combination of S-1 and S-2 features resulted in RMSE = 62.88 Mg·ha^{-1} (19.77%) that was improved to RMSE = 51.27 Mg·ha^{-1} (16.12%) when $\mathrm{FH_{imp}}$ included. This study highlighted the capability of TanDEM-X InSAR coherence with certain geometry for FH prediction. Also, the importance of FH in AGB predictions can stimulate further attempts aiming at higher spatiotemporal accuracies.**

***Index Terms*—Machine learning, multispectral, random volume over ground (RVoG), sinc model, single-pass.**

I. Introduction

Forests are one of the most important terrestrial ecosystems and impact climate change mitigation, the global carbon cycle, and human life [1], [2], [3]. However, obtaining accurate and up-to-date information about forest structural attributes, especially forest height (FH), is challenging [4]. FH can be used in wood volume, form factor, yield tables, and site index estimation [5], [6], [7]. Moreover, it relates to aboveground biomass (AGB) via allometric equations [8]. AGB is the largest carbon pool directly influenced by deforestation and forest degradation [9], [10]. Moreover, it is needed for the ecological modeling of forests and productivity [11]. Thus, developing accurate ways for monitoring and predicting AGB is important.

Field measurements of FH are time-consuming and costly, and AGB is even impractical [5], [12], [13]. In addition, field measurements are often insufficient to provide up-to-date information on the extent, spatial distribution, and temporal changes of forest cover over large areas [14], [15], [16]. Therefore, the implementation of a more economical source of data is needed [17]. Currently, various space-borne sensors provide an appropriate source of information for predicting and mapping forest attributes [5], [13], [18]. Optical sensors have been intensively used for AGB prediction across different study areas [19], [20], [21], [22], [23], [24]. However, the reflectance comes from the top of the forest canopy while the AGB is concentrated in tree stems mostly [13]. Synthetic aperture radar (SAR) is a useful instrument with the ability to penetrate the vertical structure of forests due to its long wavelength. SAR sensors provide a wall-to-wall source of data not affected by weather conditions that are comparable with optical remote sensing [15], [17], [25], [26]. The lack of systematic and consistent field measurements makes the estimates of large-area AGB maps unreliable. However, Santoro and Cartus [27] is a known example where Sentinel-1, Envisat, ALOS-1, and -2 satellites, along with additional information from earth observation sources were used in creating

Manuscript received 9 October 2023; revised 6 January 2024; accepted 23 March 2024. Date of publication 1 April 2024; date of current version 19 April 2024. This work was supported in part by the DLR for the TanDEM-X data that used in this study under science proposals NTI_INSA1194 and NTI_POLI2174 and in part by the Iran National Science Foundation (INSF) under Grant 97011637. *(Corresponding author: Ghasem Ronoud.)*

Ghasem Ronoud is with the School of Forest Sciences, University of Eastern Finland, FI-80101 Joensuu, Finland, and also with the Department of Forestry and Forest Economics, Faculty of Natural Resources, University of Tehran, Karaj 14176-43184, Iran (e-mail: ghasem.ronoud@uef.fi).

Ali A. Darvishsefat is with the Department of Forestry and Forest Economics, Faculty of Natural Resources, University of Tehran, Karaj 14176-43184, Iran (e-mail: adarvish@ut.ac.ir).

Maryam Poorazimy is with the School of Forest Sciences, University of Eastern Finland, FI-80101 Joensuu, Finland (e-mail: maryam.poorazimy@uef.fi).

Erkki Tomppo is with the Department of Forest Sciences, University of Helsinki, FI-00014 Helsinki, Finland (e-mail: erkki.tomppo@helsinki.fi).

Oleg Antropov is with the VTT Technical Research Centre of Finland, 00076 Espoo, Finland (e-mail: oleg.antropov@vtt.fi).

Jaan Praks is with the Department of Electronics and Nanoengineering, School of Electrical Engineering, Aalto University, 02150 Helsinki, Finland (e-mail: jaan.praks@aalto.fi).

Digital Object Identifier 10.1109/JSTARS.2024.3383777

a global AGB map. Generally, SAR techniques were used for characterizing forest structures with two different approaches that are direct interpretation of backscattered SAR signal and interpretation of interferometric SAR (InSAR) measurements [4]. The first approach usually exhibits signal saturation, especially in a forest with high biomass. The level of observed saturation depends on the sensor wavelength, polarization, local climate, weather conditions, and forest structure itself [13]. In the second method, one interferometric pair of images is used for deriving FH that can be further used in AGB prediction [28], [29]. This method has the potential to overcome the saturation problem of the first one [30].

Many studies have demonstrated the potential of InSAR coherence, phase, and their combination in FH prediction [31], [32], [33], [34]. Also, reliable predictions have been obtained by model-based methods including the random volume over ground (RVoG) model at different site conditions [35], [36], [37], [38]. However, deriving FH from InSAR coherence introduces challenges. First, temporal decorrelation is caused by current space-borne systems mostly offering repeat-pass InSAR data. Second, the poor availability of fully-polarimetric SAR data and/or high-accuracy digital elevation model (DEM) is another limiting factor. Finally, the computational complexity of FH inversion from scattering models makes it complicated [4]. The bistatic terraSAR-X add-on for digital elevation measurement (TanDEM-X) is the only current single-pass space-borne interferometer allowing to neglect of temporal decorrelation. Previous studies showed its sensitivity to FH prediction in boreal and tropical forests [29], [39], [40]. Also, utilizing simplified semi-empirical models was found useful to avoid some of the above-mentioned limitations [28], [37], [41], [42], [43]. Olesk et al. [4] proposed four semi-empirical coherence-based models for FH retrieval prediction using TanDEM-X data in the Hemiboreal forests of Estonia. All models exhibited a strong relationship between InSAR coherence and FH following the RVoG model. Another study investigated the effect of season on FH prediction in the same study area [4]. Schlund and Boehm [44] addressed the prediction of FH and AGB using TanDEM-X coherence data and semi-empirical models in tropical areas. They found that FH and AGB can be predicted with relative root mean square error (rRMSE) of 16% and 21% respectively. In another study, Gómez et al. [42] showed the potential of TanDEM-X coherence data and semi-empirical models for FH prediction in the Mediterranean Forests of Spain by R^2 of 0.91 and root mean square error (RMSE) of 1.24 m. However, the mentioned accuracy was limited to slopes below 10°. Chen et al. [45] indicated that the single-pass X-band interferometric coherence data and the sinc model were able to predict FH with $R^2 > 0.75$ and residual errors of approximately 2.9 m in Canada.

In this study, we aimed to enhance FH and AGB predictions by the synergistic use of single-pass TanDEM-X, Sentinel-1 (S-1), and Sentinel-2 (S-2) datasets in a highly diverse broadleaved forest of Iran. The lack of accurate DEM and the unavailability of fully polarimetric SAR data are the reasons that have stimulated attempts at FH prediction using InSAR coherence. Accordingly, two simplified semi-empirical models obtained from RVoG including the sinc and the linear models were used to show the dependency of InSAR coherence with FH in the leaf-off conditions. To improve the FH prediction accuracy (FH_{imp}), Sentinel-1 (S-1) backscatter coefficients and polarization indices and Sentinel-2 (S-2) multispectral bands, biophysical parameters, and vegetation indices were included in the analysis separately and in combination. The AGB was also predicted using the extracted features from S-1 and S-2 individually and in combination, and further improved by including FH_{imp}. We also compared the accuracy of three machine learning methods *k*-nearest neighbor (*k*-NN), random forest (RF), and support vector regression (SVR) in predicting FH and AGB. Our results addressed the potential of TanDEM-X data for FH prediction and its importance on AGB accuracies.

TABLE I
SUMMARY OF PLOT-LEVEL FIELD DATA

Variable	Min	Max	Mean	Std.
Mean dbh (cm)	18.20	91.70	45.60	11.40
Mean height (m)	17.86	35.81	27.54	4.92
Mean volume (m^3)	29.28	71.49	48.94	11.87
Number of trees (n)	8.00	73.00	19.00	8.44

II. Materials and Methods

A. Study Area

This study was conducted in an area of 800 ha of the Gorazbon and Chelir districts of Kheyruod forest, Northern Iran (see Fig. 1). The forest has been managed by the University of Tehran since 1941 and includes broadleaved, mixed, and uneven-aged structures. Our study area is bounded by the longitude of 51°.32′–51°.43′ E, and latitudes of 36°.27′–36°.40′ N. The mean elevation ranges from 1200 to 1400 m above sea level. *Fagus orientalis*, *Carpinus betulus*, *Acer* sp., and *Alnus subcordata* are the dominant species in the area.

B. Field Data

To investigate the potential of TanDEM-X data in characterizing forest structure, it is necessary to augment it with field measurements. We employed a random sampling approach across the study area; 125 square sample plots with an area of 900 m^2 (30 m × 30 m) were established. The field inventory was carried out in July 2018. Tree species, diameter at breast height (DBH), and height of all trees with DBH larger than 7.5 cm were recorded. DBH and height were measured by caliper and TruPulse 360 laser range finder respectively. The exact location of each sample plot was recorded by the Trimble R3 differential global positioning system using postprocessing kinematics. Table I presents the descriptive statistics of the plot-level field data.

In this study, Lorey's mean height was used to calculate FH predictions at sample plots. It is calculated as the average height of individual trees weighted by their basal area (1). Many studies have shown Lorey's mean height as an appropriate indicator of height in un-even aged forest stands and relevant to the volumetric height measured by SAR data [7], [46]. Notably, Lorey's mean height is less affected by the thinning and mortality

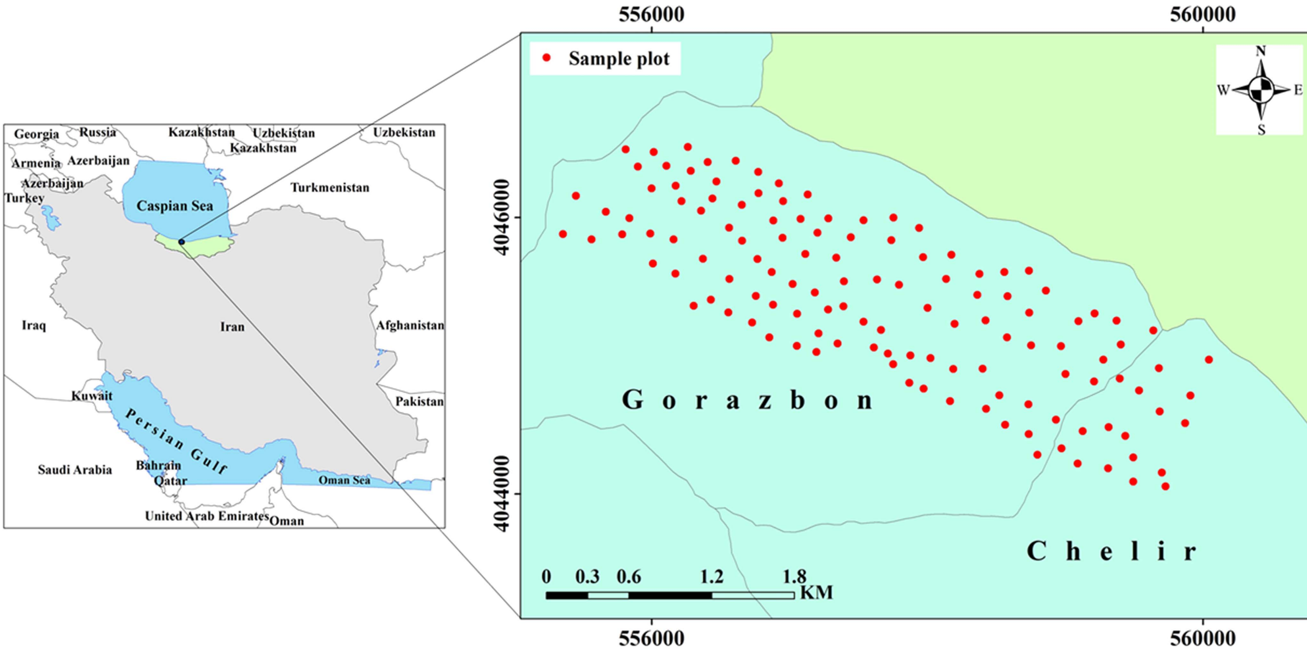

Fig. 1. Location of study area in the north of Iran (left) and distribution of in-situ sample plots (right).

of smaller trees [47], [48]

$$h_{\text{lorey}} = \frac{\sum_i^n g_i \times h_i}{\sum_i^n g_i} \quad (1)$$

where g_i refers to the basal area of ith tree (m^2) and h_i is the height of the tree (m).

The world equation was used to predict AGB based on existing volume data [49]. We used official multispecies single-entry volume tables for calculating each individual tree volume [50]. It is denoted as Tariff with DBH being used as the entry to table (2)–(4)

$$Fagus\ orientalis: v = 0.000498d^{2.215} \quad R^2 = 0.996 \quad (2)$$

$$Carpinus\ betulus: v = 0.000023d^{1.0432} \quad R^2 = 0.999 \quad (3)$$

$$Other\ species: v = 0.00133d^{1.974} \quad R^2 = 0.994 \quad (4)$$

where v is the stem volume (m^3) and d is dbh (cm). Then, the inventoried tree volume was converted to the AGB (5) by its multiplication into species-specific wood-critical density (WCD) [51], [52]. WCD is defined as the oven-dry mass per unit of green volume [52] that is 0.56, 0.68, 0.57, and 0.57 Mg·m^3 for *Fagus orientalis*, *Carpinus betulus*, *Acer* sp., and *Alnus subcordata*, respectively [51], [53].

$$\text{AGB} = \text{Volume} \times \text{WCD} \quad (5)$$

where AGB is the aboveground tree biomass (Mg), Volume is the inventoried volume of tree (m^3), and WCD refers to wood critical density (Mg·m^{-3}). It is worth mentioning that plot-level AGB was obtained by summing up all individual trees AGB per plot. Table II shows the summary statistics of Lorey's mean height and AGB across the sample plots. (For more information, see Table XII and Fig. 9 in the Appendix).

TABLE II
SUMMARY STATISTICS OF THE FIELD MEASURED LOREY'S MEAN HEIGHT AND FOREST AGB

Variable	Min	Mean	Max	Std.
Lorey's mean height (m)	21.33	34.54	47.89	5.25
AGB (Mg·ha^{-1})	191.68	320.86	468.66	77.87

The minimum (MIN), mean, maximum (MAX), and standard deviation (STD.) are reported.

TABLE III
GENERAL CHARACTERISTICS OF TANDEM-X DATA

Date	Polarization	Look angle (°)	HoA (m)
08.02.2014	HH	42.66	53.4

C. TanDEM-X Data and Processing

Interferometric TanDEM-X data was acquired at stripmap mode with HH polarization in February 2014. The image was collected during the leaf-off season with the descending pass, the effective baseline of 102.9 m, and the height of ambiguity (HoA) of 53.4 m (Table III). The product was delivered in a co-registered single-look slant range complex (CoSSCs) format with azimuth and range spacing of 2.16 m and 1.36 m.

The sentinel application platform (SNAP) software was used for interferogram generation and calculating complex interferometric coherence. The flat-earth and topography-induced phases were subtracted from the interferogram using an AlOS PALSAR DEM with a resolution of 12.5 m. Interferometric coherence explains the degree of similarity between corresponding pixels of two images and is defined by the absolute value of InSAR coherence ranges between 0 and 1 representing the weak and strong correlation between two images respectively as follows:

$$\gamma = \frac{|\langle S_1 S_2^* \rangle|}{\sqrt{\langle S_1 S_1^* \rangle \langle S_2 S_2^* \rangle}}, \; 0 \leq \gamma \leq 1 \tag{6}$$

where γ denotes the complex interferometric coherence, S_1 and S_2 are signals received at either end of the bassline, $*$ refer to complex conjugation, $|\ |$ indicates the magnitude of complex data, and $<... >$ presents the expected value averaged over a spatial window [54]. In this study, the boxcar window algorithm with the size of 10 × 10 pixels was used to predict coherence. Finally, the range Doppler terrain correction method was applied by utilizing AlOS PALSAR 12.5 m DEM [55]. The average of coherence corresponding to each sample plot was extracted for further analysis.

1) RVoG-Based Semi-Empirical Models: RVoG is one of the common scattering models defining coherence as a function of FH [56]. However, it needs more parameters to retrieve FH, which entails the use of fully polarimetric SAR or high-accuracy DEM data [57]. The RVoG model simplification proposed by Olesk et al. [4] can be an alternative in the case of single-polarized TanDEM-X data. It resulted in a set of semi-empirical models containing a physical-based framework for the use of InSAR coherence in FH9 retrieval. Accordingly, two semi-empirical models of sinc and linear based on the assumptions of neglecting extinction and ground reflection were used to retrieve $\mathrm{FH_{Sinc}}$ and $\mathrm{FH_{Lin}}$ respectively. The sinc model represents the trigonometric function sin*(x)/x* and the $\mathrm{FH_{Sinc}}$ can be inverted afterward (7). Similarly, the linear model was constructed to make a linear relation between $\mathrm{FH_{Lin}}$ and interferometric coherence as (8)

$$|\gamma| = 0.95 \text{ Sinc } \left(C_{\mathrm{Sinc}} \pi \frac{\mathrm{FH_{Sinc}}}{\mathrm{HoA}} \right) \tag{7}$$

$$|\gamma| = 1 - \frac{\mathrm{FH_{Lin}}}{\mathrm{HoA}} C_{\mathrm{lin}} \tag{8}$$

where $|\gamma|$ is the coherence amplitude, $\mathrm{FH_{Sinc}}$ and $\mathrm{FH_{Lin}}$ refer to the FH (m) derived from sinc and linear models respectively, and HoA is the height corresponding to an interferometric phase change of 2π (m). These models introduce empirical parameters of C_{Sinc} and C_{lin} as well.

D. Sentinel Data and Processing

The copernicus open access data including Sentinel-1 (S-1) and Sentinel-2 (S-2) were used in this study. The C-band S-1 data was acquired in descending pass on 31 July 2018 corresponding to the field inventory campaign. It was collected in the Interferometric Wide Swath mode with two polarization channels of VV and VH. The acquisition range of incidence angle was between 30.92° and 46.32°. Similarly, the cloud-free S-2 data was delivered in Level-1C on 25 September 2018. All the S-1 and S-2 data processing were performed using SNAP software as described in the following.

S-1 data was processed to obtain radiometrically terrain-flattened (gamma-naught) backscatter coefficients γ° in VV and VH polarizations. To accomplish this, the VV and VH intensities were converted to γ° using radiometric normalization according to the local incidence angle, filtered for speckle noise by refined Lee algorithm [58], and converted to *dB* (see Table IV). Finally, the range-Doppler terrain correction was applied for the geocoding. For this purpose, the 12.5 m AlOS PALSAR DEM was utilized [55]. In addition, five polarization indices of the ratio (VH/VV), the difference (VH-VV), multiplication (VH×VV), mean ((VH + VV)/2), and square root ($\sqrt{\mathrm{VH} \times \mathrm{VV}}$) were calculated as predictor features (see Table IV) [23], [59], [60].

To process S-2 data, a SEN2COR atmospheric processor was applied to convert the S-2 Level-1C top-of-atmosphere into the S-2 level-2A bottom-of-atmosphere product [61]. Out of the 13 spectral bands, 4 visible and near-infrared, 3 red edges, and 3 short-wavelength infrared bands were extracted for further pre-processing (see Table IV) [62]. The existing 12.5 m DEM of ALOS PALSAR was used to assess the geometric accuracy of S-2 images. In addition to main spectral bands, twelve vegetation indices and five biophysical parameters including leaf area index (LAI), leaf chlorophyll content (Cab), canopy water content (CWC), fraction of absorbed photosynthetically active radiation (FAPAR), and fractional vegetation cover (FCOVER) were calculated (see Table IV). The computation of biophysical products using reflectance images of S-2 was performed through the application of the “L2B biophysical processor” (version 1.1) [59], [63]. It has been developed using a training neural network algorithm over the PROSAIL radiative transfer model [64], [65].

E. Machine Learning Methods

In this study, three machine learning methods of *k*-NN, RF, and SVR were used to predict FH and AGB. The caret (classification and regression training) package of *R* was used to implement methods [77] described further.

k-NN method is often used for predicting forest structural characteristics and for small-area estimation with the help of auxiliary remote sensing data [78], [79], [80]. To predict the value of the unknown response variable, a linear combination of *k* known observations, nearest in the feature space, is calculated. In this study, a rectangular kernel with *k* varying between 1 and 20 was tested. Moreover, the capability of four distance metrics was evaluated, namely Euclidean, Euclidean Squared, Chebyshev, and Manhattan.

RF method is one of the common nonparametric methods in forest studies that is based on regression trees [13], [81], [82]. This method is known for its potential to reduce systematic errors and overfitting [83]. In other words, the regression trees continue to grow until a minimum error of response features is achieved. We determined the optimal *k* predictors in a range of the square root of the predictor features number ±2. The number of decision trees was set to 500.

SVR is one of the nonparametric methods that assumes a unique relationship between each set of predictor and response features. For grouping among predictor features, the hyperplanes in multidimensional space will be built from the predictor features acting as axes [84]. We considered four different kernels of

TABLE IV
LIST OF S-1 AND S-2 PREDICTOR FEATURES USED FOR PREDICTING FH AND AGB

Mission		Predictor feature	Description/Resolution
Sentinel-1	Polarization	VV	Vertical transmit-vertical channel
		VH	Vertical transmit-horizontal channel
	Polarization indices	VH/VV	The ratio of VH and VV
		VH-VV	Difference between VH and VV
		VH×VV	Multiplication between VH and VV
		(VH + VV)/2	Mean of VH and VV
		$\sqrt{VH \times VV}$	The square root of VH and VV
Sentinel-2	Multispectral Bands	Blue band (B2)	0.458–0.523 μm/10 m
		Green band (B3)	0.543–0.578 μm/10 m
		Red band (B4)	0.650–0.680 μm/10 m
		Red-edge 1 (RE1) (B5)	0.698–0.713 μm/20 m
		Red-edge 2 (RE2) (B6)	0.733–0.748 μm/20 m
		Red-edge 3 (RE3) (B7)	0.773–0.793 μm/20 m
		Near-infrared (NIR) (B8)	0.785–0.900 μm/10 m
		Near-infrared narrow (NIRn) (B8A)	0.855–0.875 μm/20 m
		Short wave infrared 1 (SWIR1) (B11)	1.565–1.655 μm/20 m
		Short wave infrared 2 (SWIR2) (B12)	2.100–2.280 μm/20 m
	Vegetation Biophysical Features	LAI	Leaf Area Index
		Cab	Chlorophyll content in the leaf
		CWC	Canopy water content
		FAPAR	Fraction of absorbed photosynthetically active radiation
		FCOVER	Fraction of vegetation cover
	Vegetation Indices	Difference Vegetation Index (DVI) [66]	[NIR (B8)–Red (B4)]
		Normalized Difference Vegetation Index (NDVI) [67]	[NIR (B8)–Red (B4)] / [NIR (B8) +Red (B4)]
		Green Normalized Difference Vegetation Index (GNDVI) [68]	[NIR (B8)– Green (B3)] / [NIR (B8) + Green (B3)]
		Infrared Percentage Vegetation Index [69]	[NIR (B8)/ (NIR (B8) + Red (B4))]/(NDVI+1)
		Ratio Vegetation Index (RVI) [70]	[NIR (B8) / NIR (B8)]
		Global Environmental Monitoring Index [71]	[n(1-0.25n)–(Red (B4)-0.125/1– Red (B4))]
		Meris Terrestrial Chlorophyll Index (MTCI) [72]	[RE2 (B6)– RE1 (B5)] / (RE1 (B5) + Red (B4)]
		Red-Edge Inflection Point Index [73]	700 + 40*[(((Red (B4)+RE3 (B7))/2)– RE1 (B5))/(RE2 (B6)– RE1 (B5))]
		Normalized Difference Index [74]	[RE1 (B5)–Red (B4)]/[RE1 (B5)+ Red (B4)]
		Pigment Specific Simple Ratio [75]	[RE3 (B7)–Red (B4)]/[RE1 (B5)/RE2 (B6)]
		Sentinel-2 Red-Edge Position Index [76]	705 + 35*[(((Red (B4)–RE3 (B7))/2)– RE1 (B5))/(RE2 (B6)– RE1 (B5))]
		Inverted Red-Edge Chlorophyll Index (IRECI) [76]	[RE3 (B7)/Red (B4)]

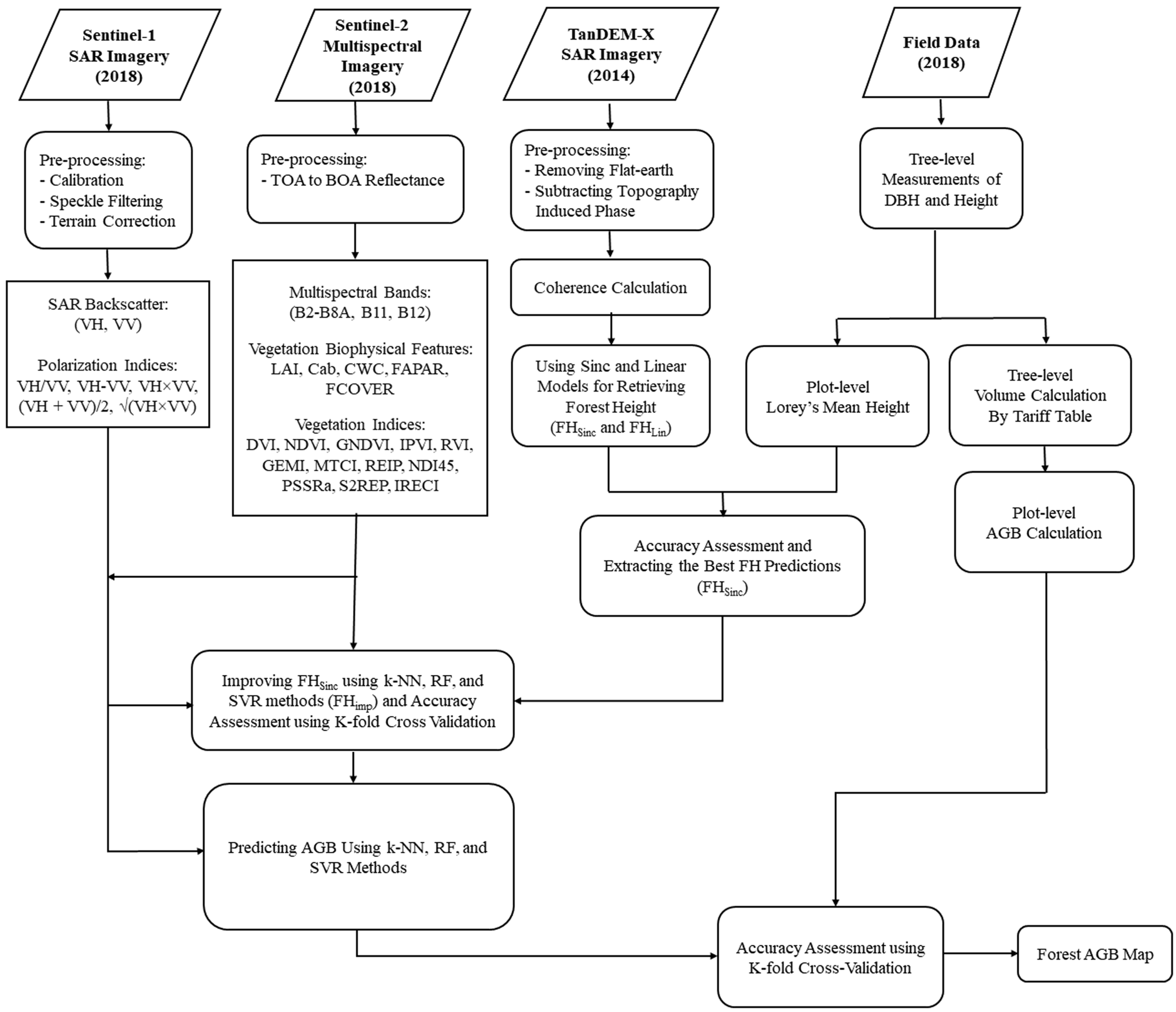

Fig. 2. Flowchart of applied methodology to predict FH and AGB.

linear, polynomials degrees 2 and 3, radial basis function (RBF), and sigmoid in terms of prediction accuracy.

F. Accuracy Assessment

A repeated K-fold cross-validation approach was used in model training and validation. The data were randomly split into $K = 5$ folds with a size of 25 per iteration where the training is carried out on K-1 folds while the remaining fold is used for the validation. The procedure was repeated up to three times generating K performance scores. The mean of generated scores defines the performance of the model. The coefficient of determination (R^2), RMSE, rRMSE, mean absolute error (MAE), and relative MAE (rMAE) were used for evaluating the predictions (9)–(13)

$$R^2 = 1 - \left(\frac{\sum_{i=1}^{n} (O_i - P_i)^2}{\sum_{i=1}^{n} (O_i - \bar{O})^2} \right) \tag{9}$$

$$\mathrm{RMSE} = \left[n^{-1} \sum_{i=1}^{n} (P_i - O_i)^2 \right]^{1/2} \tag{10}$$

$$\mathrm{rRMSE} = \frac{\mathrm{RMSE}}{\bar{O}} \times 100 \tag{11}$$

$$\mathrm{MAE} = \frac{\sum_{i=1}^{n} |P_i - O_i|}{n} \tag{12}$$

$$\mathrm{rMAE} = \frac{\mathrm{MAE}}{\bar{O}} \times 100 \tag{13}$$

where n is the number of sample plots, O_i is the observed value, P_i is the predicted value, and $\bar{O}$ refers to the mean of observed values. Fig. 2 depicts the methodology flowchart.

III. Results

A. Predicting FH Using TanDEM-X InSAR Coherence

Results of linear and sinc semi-empirical models in FH prediction indicate that the sinc model had better performance in comparison with the linear model with $R^2 = 0.45$ and rRMSE = 12.39% (see Table V). The scatterplot of observed versus $\mathrm{FH}_{\mathrm{Sinc}}$ predicted by the sinc model is presented in Fig. 3.

TABLE V
RESULT OF FH PREDICTION BASED ON SEMI-EMPIRICAL MODELS

Model	C Parameter	RMSE (m)	rRMSE (%)	(R^2)
Sinc	1.1	4.28	12.39	0.45
Linear	1	5.40	15.63	0.29

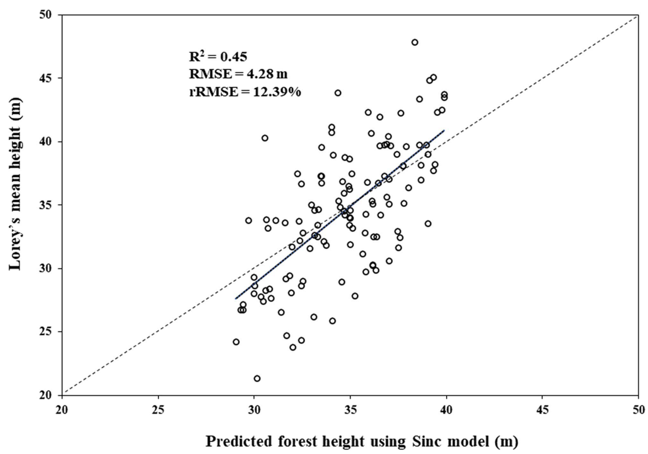

Fig. 3. Observed versus predicted FH using the sinc model (FH_{Sinc}).

B. Improved FH Prediction (FH_{imp}) by the Inclusion of S-1 and S-2 Data

To improve the FH_{Sinc} predictions, S-1 and S-2 predictor features were also included separately and in combination. Tables VI–VIII show the FH_{imp} predictions provided by k-NN, RF, and SVR machine learning methods, respectively. Here, the combination of FH_{Sinc} and S-2 was more accurate than the combination with S-1 data for FH_{imp} prediction. The obtained rRMSE for k-NN, RF, and SVR methods were 10.91%, 10.74%, and 10.36% respectively.

In general, the combination of FH_{Sinc}, S-1, and S-2 achieves the highest accuracy in FH_{imp} prediction compared to other combinations of datasets. The SVR method with RBF kernel produced the best results with R^2 of 0.59 and RMSE of 3.18 m (rRMSE = 9.21%). A scatter plot of observed Lorey's mean height against predicted FH_{imp} using the SVR method has been illustrated in Fig. 4.

C. AGB Prediction and Validation

The AGB prediction was examined using two different approaches. First, AGB was predicted using S-1 and S-2 predictors separately and then in combination. Second, the gain in accuracy was evaluated for a scenario when FH_{imp} was combined with the abovementioned datasets. Tables IX–XI show the results of AGB prediction using k-NN, RF, and SVR, respectively. Generally, S-2 showed more accurate results than S-1 for AGB prediction (RMSE = 65.51 Mg·ha^{-1}, rMAE = 17.03%, $R^2 = 0.37$). The errors decreased when using both S-1 and S-2 with the RF method ($R^2 = 0.40$ and RMSE = 62.88 Mg·ha^{-1}).

The RF model, combining FH_{imp} and features from S-1 and S-2 as predictors, reduced errors in AGB predictions with

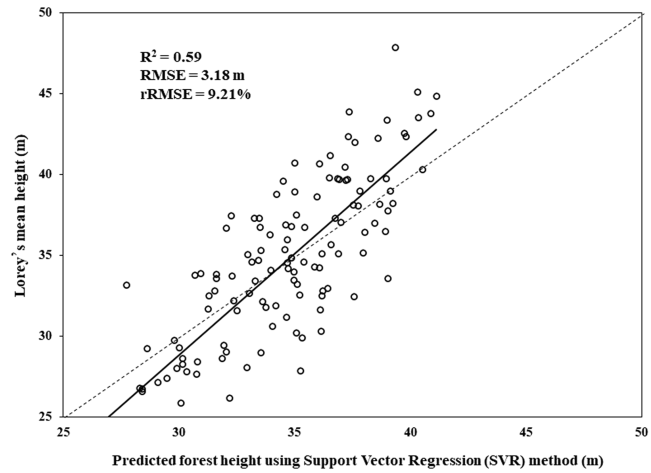

Fig. 4. Observed versus improved FH (FH_{imp}) predicted by SVR method.

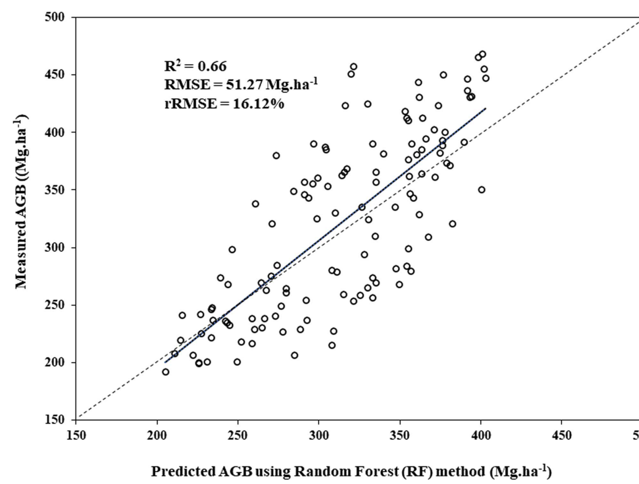

Fig. 5. Scatterplot of measured versus predicted AGB using the RF method and a combination of S-1, S-2, and FH_{imp}.

$R^2 = 0.66$ and rRMSE of 16.12%. Fig. 5 shows the scatterplot of measured versus predicted AGB using the best model. The final AGB map was also created by applying that model to the whole study area [see Fig. 6(a)]. For comparison reasons, the global AGB map in 2018 corresponding to our study area resampled to 30 m is presented in Fig. 6(b) (See Santoro and Cartus [27]). It was created in a 100 m resolution using S-1 and ALOS-2 as a part of the European Space Agency's Climate Change Initiative program. Based on the visual comparison, a minor spatial agreement existed between our AGB map and the Santoro and Cartus [27] map, particularly in areas with lower AGB. While the effect of AGB saturation in the Santoro and Cartus [27] map was clearly observed (see Fig. 6).

IV. DISCUSSION

This study focused on the syringic use of TanDEM-X single-polarized, S-1, and S-2 datasets to predict the FH and AGB of trees. The FH predictions were first obtained using semi-empirical models of linear and sinc derived from the RVoG

TABLE VI
RESULTS OF THE *K*-NN METHOD FOR IMPROVING FH PREDICTIONS (FH_{IMP})

Dataset	**Distance**	**k max**	**RMSE (m)**	**rRMSE (%)**	**(R^2)**	**MAE (m)**	**rMAE (%)**
FH_{Sinc} + Sentinel-1	Euclidean	8	4.48	12.97	0.43	3.57	10.33
	Euclidean Squared	7	4.53	13.11	0.41	3.61	10.45
	Manhatan	15	4.55	13.17	0.42	3.64	10.54
	Chebychev	6	4.28	12.39	0.49	3.42	9.90
FH_{Sinc} + Sentinel-2	Euclidean	11	3.77	10.91	0.50	2.95	8.54
	Euclidean Squared	12	3.88	11.23	0.47	3.10	8.97
	Manhatan	15	3.81	11.03	0.43	3.27	9.47
	Chebychev	6	3.81	11.03	0.49	3.01	8.71
FH_{Sinc} + Sentinel-1 + Sentinel-2	Euclidean	11	3.54	10.25	0.49	2.64	7.64
	Euclidean Squared	5	3.53	10.22	0.48	2.61	7.56
	Manhatan	6	3.49	10.10	0.53	2.61	7.56
	Chebychev	6	3.49	10.10	0.52	2.63	7.61

TABLE VII
RESULTS OF THE RF METHOD FOR IMPROVING FH PREDICTIONS (FH_{IMP})

Dataset	**Optimal number of trees**	**Number of predictors (k)**	**RMSE (m)**	**rRMSE (%)**	**(R^2)**	**MAE (m)**	**rMAE (%)**
FH_{Sinc} + Sentinel-1	500	1	4.28	12.39	0.46	3.41	9.87
	500	2	4.29	12.42	0.48	3.39	9.81
	500	3	4.18	12.10	0.50	3.29	9.52
	500	4	4.21	12.19	0.49	3.31	9.58
	500	5	4.22	12.22	0.49	3.33	9.64
FH_{Sinc} + Sentinel-2	500	3	3.86	11.17	0.48	3.04	8.80
	500	4	3.71	10.74	0.51	3.03	8.77
	500	5	3.72	10.77	0.50	3.07	8.89
	500	6	3.72	10.77	0.50	3.07	8.89
	500	7	3.80	11.00	0.48	3.15	9.12
FH_{Sinc} + Sentinel-1 + Sentinel-2	500	4	3.62	10.48	0.51	2.81	8.13
	500	5	3.40	9.84	0.54	2.63	7.61
	500	6	3.35	9.70	0.55	2.59	7.50
	500	7	3.32	9.61	0.54	2.54	7.35
	500	8	3.31	9.58	0.58	2.52	7.29

model. We found the sinc model to be more accurate than the linear model in predicting FH (RMSE of 4.28 m and R^2 of 0.45) in the broadleaved forest of Iran (see Table V), which is in line with the results obtained by Praks et al. [6] in Hemiboreal forest. It decreased the rRMSE by 3.24% when compared with the Linear model (see Table V), although, the acceptable performance of both linear and sinc models for FH prediction has been reported in previous studies [4], [47]. It is worth mentioning that the FH prediction accuracy largely depends on the HoA which is 53.4 m in our case. According to [42] and [45], the sensitivity of InSAR coherence to FH changes would be optimum when the FH ranges between 1/3 of HoA and HoA. Praks et al. [6] also recommended that the HoA should be around twice the height of forest stands. Hence, further experimental research on the effect of acquisition geometry like HoA on FH predictions is needed. Moreover, the local slope is a potential parameter affecting FH accuracies. Gómez et al. [42] have indicated the higher accuracy of the sinc model for FH predictions in the areas with a slope of fewer than 10° in Mediterranean forests. They achieved the best RMSE of 1.24 m and R^2 of 0.91 for FH predictions. Considering the mountainous condition of the Hyrcanian forest of Iran, the slope can be a limiting parameter for large-scale FH mapping. The complexity of the stands and the existence of multispecies can affect the attention rate of the vegetation layer and ground reflectivity. Second, FH_{sinc} predictions were improved by its combination with Sentinel-1 (S-1) and Sentinel-2 (S-2) datasets

TABLE VIII
RESULTS OF THE SVR METHOD FOR IMPROVING FH PREDICTIONS (FH_{IMP})

Dataset	Kernel	RMSE (m)	rRMSE (%)	(R^2)	MAE (m)	rMAE (%)
FH_{Sinc} + Sentinel-1	Linear	4.30	12.45	0.47	3.39	9.81
	Polynomial	4.28	12.39	0.48	3.33	9.64
	Radial Basis Function kernel (RBF)	4.35	12.59	0.46	3.43	9.93
	Sigmoid	4.29	12.42	0.47	3.35	9.70
FH_{Sinc} + Sentinel-2	Linear	3.83	11.09	0.47	3.39	9.81
	Polynomial	3.59	10.39	0.55	3.24	9.38
	Radial Basis Function kernel (RBF)	3.61	10.45	0.53	3.29	9.52
	Sigmoid	3.58	10.36	0.55	3.24	9.38
FH_{Sinc} + Sentinel-1 + Sentinel-2	Linear	3.67	10.62	0.47	3.44	9.96
	Polynomial	3.22	9.32	0.58	3.19	9.23
	Radial Basis Function kernel (RBF)	3.18	9.21	0.59	3.18	9.21
	Sigmoid	3.20	9.26	0.58	3.19	9.23

TABLE IX
RESULTS OF THE k-NN METHOD FOR AGB PREDICTION

Dataset	Distance	k max	RMSE ($Mg.ha^{-1}$)	rRMSE (%)	(R^2)	MAE ($Mg.ha^{-1}$)	rMAE (%)
Sentinel-1 / Sentinel-1 + FH_{imp}	Euclidean	20/19	83.15/77.67	26.14/24.42	0.03/0.28	73.50/68.53	23.11/21.55
	Euclidean Squared	19/19	83.35/77.75	26.21/24.45	0.02/0.28	73.36/68.63	23.07/21.58
	Manhatan	20/20	83.66/77.97	26.30/24.52	0.03/0.29	74.18/69.07	23.32/21.72
	Chebychev	19/19	83.35/78.35	26.21/24.64	0.02/0.28	73.36/68.49	23.07/21.54
Sentinel-2 / Sentinel-2 + FH_{imp}	Euclidean	7/7	68.86/58.98	21.65/18.54	0.31/0.57	55.89/46.05	17.57/14.48
	Euclidean Squared	11/8	69.70/62.23	21.92/19.57	0.29/0.50	57.57/49.87	18.10/15.68
	Manhatan	12/7	68.64/59.65	21.58/18.76	0.32/0.56	57.08/46.74	17.95/14.70
	Chebychev	12/12	68.64/58.64	21.58/18.44	0.32/0.58	57.08/47.08	17.95/14.80
Sentinel-1 + Sentinel-2 / Sentinel-1 + Sentinel-2 + FH_{imp}	Euclidean	15/11	66.03/57.89	20.76/18.20	0.36/0.61	55.29/39.91	17.38/12.55
	Euclidean Squared	19/15	67.61/57.57	21.26/18.10	0.37/0.60	56.69/41.00	17.82/12.89
	Manhatan	13/16	66.05/56.46	20.77/17.75	0.36/0.62	55.00/39.86	17.29/12.53
	Chebychev	13/13	66.05/56.05	20.77/17.62	0.36/0.63	55.00/39.00	17.29/12.26

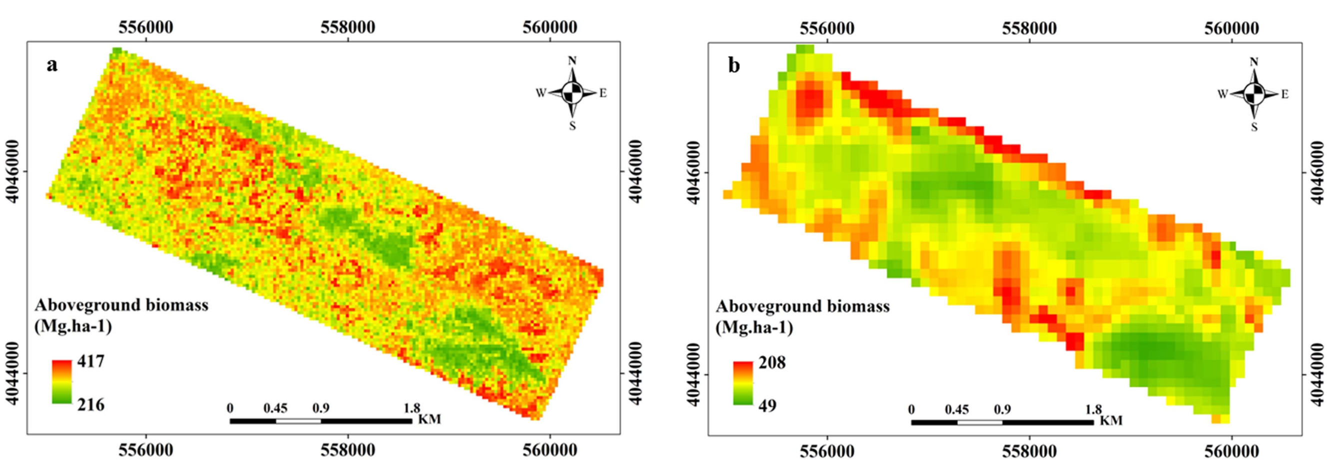

Fig. 6. (a) AGB map of this study predicted by a combination of S-1, S-2, and FH_{imp} predicted by the RF model that was trained with plot-level field data in 2018. (b) Respective global AGB map constructed by Santoro and Cartus [27].

TABLE X
RESULTS OF RF METHOD FOR AGB PREDICTION

Dataset	Optimal number of trees	Number of predictors (k)	RMSE (Mg.ha^{-1})	rRMSE (%)	(R^2)	MAE (Mg.ha^{-1})	rMAE (%)
Sentinel-1 / Sentinel-1 + FH$_{imp}$	500	1	88.89/82.44	27.95/25.92	0.02/0.28	77.28/71.88	24.30/22.60
	500	2	89.26/83.52	28.06/26.26	0.02/0.28	77.39/72.82	24.33/22.90
	500	3	89.43/83.35	28.12/26.21	0.02/0.28	77.33/72.77	24.31/22.88
	500	4	89.24/83.34	28.06/26.19	0.03/0.28	77.34/72.69	24.32/22.86
	500	5	89.06/83.31	28.00/26.19	0.03/0.28	77.24/72.68	24.29/22.85
Sentinel-2 / Sentinel-2 + FH$_{imp}$	500	3	66.77/56.75	20.99/17.84	0.34/0.60	55.60/45.51	17.48/14.31
	500	4	66.39/56.31	20.87/17.70	0.35/0.61	55.20/45.16	17.36/14.20
	500	5	65.81/56.42	20.69/17.74	0.36/0.61	54.55/45.20	17.15/14.21
	500	6	65.84/56.25	20.70/17.69	0.36/0.61	54.55/44.85	17.15/14.10
	500	7	65.51/55.91	20.60/17.58	0.37/0.62	54.16/44.62	17.03/14.03
Sentinel-1 + Sentinel-2 / Sentinel-1 + Sentinel-2 + FH$_{imp}$	500	4	63.64/52.89	20.01/16.63	0.39/0.63	52.32/41.59	16.45/13.08
	500	5	63.76/52.71	20.05/16.57	0.38/0.64	52.16/41.10	16.40/12.92
	500	6	63.61/52.44	20.00/16.49	0.39/0.64	51.94/40.85	16.33/12.84
	500	7	63.34/52.31	19.91/16.45	0.39/0.64	51.69/40.71	16.25/12.80
	500	8	62.88/51.27	19.77/16.12	0.40/0.66	51.30/39.59	16.13/12.45

TABLE XI
RESULTS OF SVR METHOD FOR AGB PREDICTION

Dataset	Kernel	RMSE (Mg.ha^{-1})	rRMSE (%)	(R^2)	MAE (Mg.ha^{-1})	rMAE (%)
Sentinel-1 / Sentinel-1 + FH$_{imp}$	Linear	87.74/79.83	27.59/25.10	0.03/0.29	75.45/64.01	23.72/20.13
	Polynomial	81.96/78.02	25.77/24.53	0.01/0.28	72.59/62.64	22.82/19.70
	Radial Basis Function kernel (RBF)	87.32/81.42	27.45/25.60	0.06/0.29	76.58/66.57	24.08/20.93
	Sigmoid	81.91/76.91	25.75/24.18	0.01/0.27	72.59/62.61	22.82/19.69
Sentinel-2 / Sentinel-2 + FH$_{imp}$	Linear	87.50/77.77	27.51/24.45	0.30/0.56	73.03/63.34	22.96/19.92
	Polynomial	67.43/57.75	21.20/18.16	0.33/0.59	57.54/48.29	18.09/15.18
	Radial Basis Function kernel (RBF)	67.30/57.70	21.16/18.14	0.34/0.59	55.38/46.14	17.41/14.51
	Sigmoid	67.62/57.95	21.26/18.22	0.33/0.58	57.62/47.95	18.12/15.08
Sentinel-1 + Sentinel-2 / Sentinel-1 + Sentinel-2- + FH$_{imp}$	Linear	84.55/67.81	26.58/21.32	0.35/0.61	69.91/58.23	21.98/18.31
	Polynomial	67.10/55.17	21.10/17.35	0.33/0.58	56.38/44.53	17.73/14.00
	Radial Basis Function kernel (RBF)	63.91/52.12	20.10/16.39	0.39/0.64	53.71/42.43	16.98/13.34
	Sigmoid	64.30/52.57	20.22/16.53	0.38/0.63	54.15/43.04	17.03/13.53

(FH$_{\mathrm{imp}}$). The RMSE was 4.18 m when FH$_{\mathrm{Sinc}}$ combined with the S-1 using RF (k = 3) and 3.58 m when FH$_{\mathrm{Sinc}}$ combined with S-2 using SVR (Sigmoid kernel) (see Tables VII and VIII). This can be attributed to the presence of speckle noise in SAR backscatters, especially in these dense forests with complex structures [85]. The presence of speckles can reduce the sensitivity of SAR signals to forest structures. Unlike optical data that capture the spectral response of the horizontal structure, SAR backscatters might be insensitive if there is a little height variation [86]. In addition, optical data provide complementary information about forest horizontal structure besides the vertical structure that has been addressed by FH$_{\mathrm{Sinc}}$ in the modeling phase [25], [87], [88]. Of importance, the high level of structural complexity in our study area (see Table I) may cause the weak performance of the S-1 due to signal saturation [89], [90]. Other site conditions such as soil moisture and roughness are also related to signal saturation [13]. Fig. 7 visually demonstrates the results of different methods and datasets for FH$_{\mathrm{imp}}$ prediction along with FH$_{\mathrm{Sinc}}$ itself.

The most accurate FH$_{\mathrm{imp}}$ prediction was obtained by adding FH$_{\mathrm{Sinc}}$ to the combination of S-1, and S-2 datasets using the SVR method (R^2 = 0.59 and RMSE = 3.18 m). Ghosh et al. [88] have reported an improved FH prediction using S-1 interferometric coherence and S-2 biophysical parameters in the mangrove forests. They obtained an RMSE of 1.57 m and R^2 of 0.60, which was superior results compared to the current study. It can be explained by the relatively flat topography in their study site with a maximum elevation of 16 m. In another study, Li et al. [18] upscaled the ICESat-2-derived FH with the Sentinels and Landsat-8 satellites in the Inner Mongolia Autonomous Region of China. They showed higher accuracy in upscaling FH assisted by Sentinel satellites in comparison with Lansat-8 data. Even

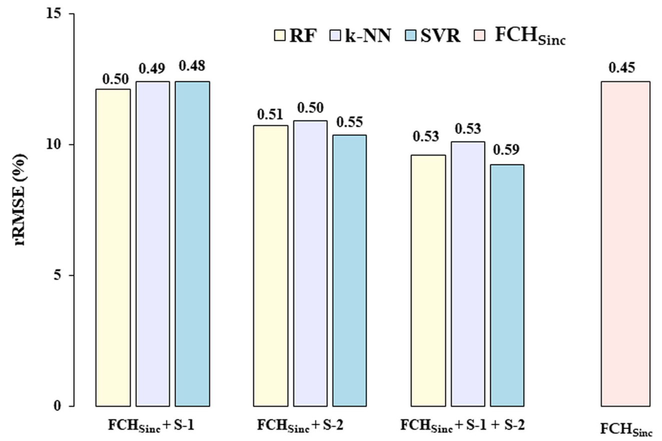

Fig. 7. General overview of the FH_{imp} prediction accuracies using the combination of different datasets including S-1, S-2, and FH_{Sinc} itself. The value on top of the bars indicates the R^2.

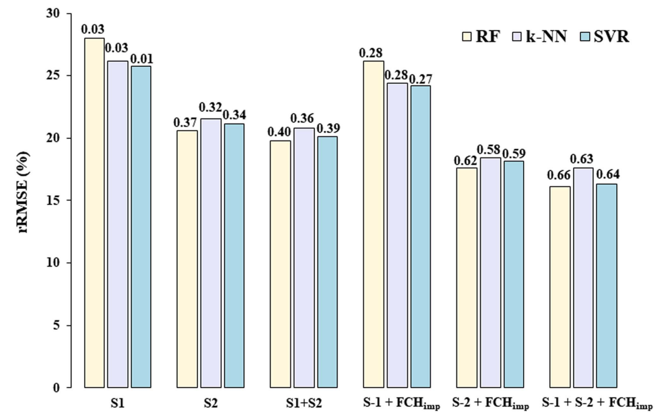

Fig. 8. General overview of the AGB prediction accuracies using the combination of different datasets including S-1, S-2, and FH_{imp}. The value on top of the bars indicates the R^2.

though the performance of prediction methods was rather similar in FH predictions in our study, SVR with the RBF kernel was the most accurate for FH predictions. It has good agreement with the study conducted by Pourshamsi et al. [91] indicating the SVR method is the best for FH predictions using a combination of polarimetric SAR and LiDAR data. SVR takes advantage of solving small-sample and nonlinear multidimensional problems, and previous studies confirm its applicability in forest studies [13], [60], [89], [92]. It is worth mentioning that our results for FH prediction were in line with other studies in the Hyrcanian forest. For instance, Pourrahmati et al. [93] resulted in $R^2 = 0.59$ and RMSE = 5.5 m for wall-to-wall mapping of FH using the synergy of ICESat/GLASS and optical images. Overall, the workflow demonstrated in this study suggests a possibility for FH prediction in the absence of highly accurate data sources such as terrestrial and airborne laser scanning as well as full polarimetric airborne SAR data.

We additionally studied the AGB prediction using the S-1, S-2, and their combination. Moreover, the precision gained by the inclusion of FH_{imp} into Sentinel-derived predictor features was quantified. We also compared the final AGB map of this study with the global AGB map generated by Santoro and Cartus [27]. The synergy of S-1 and S-2 using the RF method led to better AGB predictions than using those individually with RMSE and R^2 of 62.88 Mg·ha^{-1} and 0.40 respectively. Considering the high level of AGB in our study area, the weak performance of S-1 backscatters than S-2 was observed and can be attributed to the signal saturation [25], [90], [94]. Prior studies have also proved the capability of the combination of optical and SAR datasets for AGB predictions [13], [41], [87], [95], [96], [97]. Antropov et al. [98] addressed the combination of TanDEM-X-derived height and Landsat-8 features for predicting growing stock volume in Boreal forests ($R^2 = 0.57$ and rRMSE = 34%).

By adding FH_{imp} into AGB models based on S-1, S-2, and a combination of S-1 and S-2 datasets, the accuracy was increased (see Fig. 8), showing the importance of tree height containing a large part of woody biomass. The most accurate model was obtained using the RF method and a combination of FH_{imp} with S-1 and S-2. It decreased the AGB prediction error by RMSE of 11.61 Mg·ha^{-1}, rRMSE = 3.65%, and R^2 of 0.26 in comparison with using a combination of S-1 and S-2 only. Generally, the canopy height obtained from SAR and LiDAR data has been successfully used in AGB predictions [99], [100], [101]. The saturation level related to the mentioned model combining FH_{imp} with S-1 and S-2 exceeds 300 Mg·ha^{-1}, which is in line with Vafaei et al. [102] where a multisensorial study was conducted in the Hyrcanian forest of Iran. According to the mean decrease in the Gini index of the RF algorithm, the vegetation index of MTCI is the most important predictor in AGB prediction with the highest correlation of 0.51. With increasing MTCI, the predicted AGB also increases until the signal saturates. It is worth mentioning that utilizing the S-2 sensor with red-edge bands is known to effectively improve the saturation tendency in predictions [103], [104], [105]. Other studies also supported the primary role of optical datasets in predicting forest attributes ([106], [107]). Followed by MTCI, GNDVI, and IRECI were two other S-2 features with high relative importance in AGB predictions.

A comparison of our final AGB map with the respective global map generated by Santoro and Cartus [27] showed little correspondence in areas with lower levels of AGB. A similar conclusion was found by Santoro and Cartus [27] showing the increased variance but limited bias for AGB up to 250 Mg·ha^{-1} that caused underestimated AGB predictions. It was attributed to the limited sensitivity of used datasets and the constraint of maximum AGB that was lower than reality. Especially, the Hyrcanian forests of Iran featured as an old highly diverse forest with a large amount of AGB [25], [102], [107], [108], [109]. Particularly, their model training phase did not require in-situ observations and used SAR predictors for creating an AGB map in 2018. Accordingly, we only obtained a correlation of 0.2 between sample plots AGB and the corresponding values from the global AGB map. However, the mismatch between the global AGB map and sample plots in terms of spatial resolution causes the limited possibility of quantifying the local errors and overall bias of the global AGB map. Hence, any interpretation needs to be done with caution.

Upon the obtained results in this study, the FH has been predicted accurately due to the canopy height dependency on the interferometric coherence. It is worth mentioning that there is an approximately four-year temporal difference between TanDEM-X and field data that might affect the obtained errors. The inclusion of FH_{imp} into AGB models caused a significant improvement, however, the other sources of uncertainties might affect the predictions. These include the forest ecosystems, topography, S-1 and S-2 data, statistical errors, and propagation of FH potential errors into the AGB predictions [13], [44].

V. Conclusion

In this study, single-polarized TanDEM-X data and freely available Sentinel satellites were used to predict FH and AGB in the Hyrcanian forest of Iran. To accomplish this, semi-empirical linear and sinc models obtained from RVoG were used to predict FH and it was further improved by the inclusion of S-1 and S-2 datasets (FH_{imp}). The SVR method led to the most accurate FH_{imp} predictions with an RMSE of 3.18 m and R^2 of 0.59 when FH_{sinc} and a combination of S-1 and S-2 were used. The AGB predictions using a combination of S-1 and S-2 were also improved when FH_{imp} was included (rRMSE = 16.12% and $R^2 = 0.66$). Our results confirmed the potential of TanDEM-X data in predicting FH in the absence of fully polarimetric datasets and accurate DEM in a highly diverse Hyrcanian forest of Iran. Also, we addressed the gained precision in AGB models when FH_{imp} predictions were added to the datasets. However, further studies are encouraged using data with different acquisition geometry, and stratified forest stands based on slope and species.

Appendix

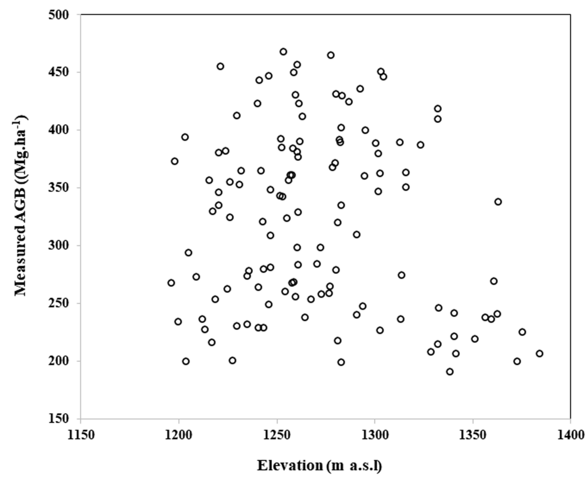

Fig. 9. Distribution of elevation and AGB at various sample plots.

TABLE XII
Lorey's Mean Height (M) / AGB (Mg·ha^{-1}) Across 125 Sample Plots

1- 38.10 / 365.74	26- 37.33 / 365.52	51- 37.30 / 238.68	76- 40.68 / 343.17	101 - 28.04 / 423.68
2- 34.31 / 274.30	27- 42.01 / 356.95	52- 36.91 / 269.36	77- 28.27 / 285.06	102 - 39.73 / 355.46
3- 21.33 / 200.98	28- 37.08 / 260.98	53- 28.64 / 424.00	78- 33.73 / 400.86	103 - 37.01 / 273.87
4- 26.57 / 229.22	29- 39.83 / 324.64	54- 39.02 / 431.09	79- 36.52 / 259.40	104 - 34.55 / 268.45
5- 35.19 / 309.07	30- 42.38 / 268.50	55- 33.61 / 335.61	80- 27.42 / 371.78	105 - 37.78 / 455.87
6- 38.77 / 357.23	31- 40.31 / 385.06	56- 31.90 / 216.57	81- 30.32 / 240.34	106 - 31.17 / 279.10
7- 28.65 / 263.45	32- 31.71 / 253.96	57- 42.28 / 230.92	82- 32.51 / 248.12	107 - 34.23 / 329.18
8- 32.22 / 325.25	33- 39.76 / 380.83	58- 35.08 / 236.77	83- 38.20 / 335.23	108 - 32.96 / 199.44
9- 36.72 / 227.98	34- 39.69 / 330.17	59- 36.75 / 234.54	84- 36.78 / 436.70	109 - 29.78 / 227.19
10- 37.30 / 280.39	35- 40.45 / 264.38	60- 34.62 / 200.58	85- 33.81 / 425.39	110 - 26.19 / 320.83
11- 35.34 / 232.40	36- 42.56 / 281.82	61- 39.59 / 346.47	86- 32.50 / 265.18	111 - 39.01 / 390.34
12 - 24.37 / 221.94	37- 34.86 / 249.39	62- 39.67 / 294.11	87- 31.59 / 343.66	112 - 37.52 / 299.10
13- 30.64 / 246.51	38- 28.10 / 241.37	63- 39.77 / 394.61	88- 35.13 / 320.96	113 - 39.75 / 412.53
14- 24.72 / 241.86	39- 26.78 / 200.21	64- 38.21 / 373.46	89- 40.74 / 382.62	114 - 33.47 / 364.11
15- 29.24 / 191.68	40- 27.83 / 206.93	65- 36.43 / 229.43	90- 33.85 / 413.03	115 - 35.35 / 350.84
16- 28.41 / 207.03	41- 27.67 / 225.75	66- 32.44 / 361.48	91- 33.58 / 361.90	116 - 32.66 / 418.94
17- 29.04 / 219.41	42- 38.14 / 236.57	67- 32.84 / 450.48	92- 37.48 / 431.87	117 - 32.82 / 410.40
18- 35.98 / 338.30	43- 26.76 / 238.56	68- 27.18 / 381.73	93- 43.55 / 392.22	118 - 29.00 / 215.15
19- 43.91 / 387.46	44- 23.80 / 208.43	69- 31.83 / 385.63	94- 34.07 / 298.65	119 - 24.25 / 269.53
20- 44.85 / 275.18	45- 29.90 / 237.04	70- 33.23 / 457.58	95- 38.96 / 465.44	120 - 29.45 / 430.71
21- 33.91 / 363.22	46- 36.81 / 446.88	71- 34.00 / 284.03	96- 43.77 / 376.99	121 - 27.88 / 390.18
22- 34.63 / 380.30	47- 38.65 / 402.81	72- 33.18 / 256.59	97- 34.69 / 279.61	122 - 35.68 / 451.43
23- 41.19 / 360.94	48- 32.56 / 218.09	73- 36.27 / 447.72	98- 42.37 / 468.66	123 - 34.26 / 389.01
24- 29.32 / 258.72	49- 43.40 / 368.70	74- 45.15 / 393.15	99- 30.24 / 353.49	124 - 25.89 / 347.13
25- 47.89 / 390.73	50- 35.14 / 254.46	75- 33.42 / 444.18	100 - 32.15 / 348.94	125 - 31.66 / 310.24

ACKNOWLEDGMENT

The authors would like to thank DLR for providing TanDEM-X data used in the study under proposals NTI_INSA1194 and NTI_POLI2174. We also express our acknowledgments to the Iran National Science Foundation (INSF) for financial support of this research under project 97011637. We thank the anonymous reviewers for their valuable comments.

REFERENCES

[1] J. Wu, J. Shi, D. Song, S. Zheng, and S. Chen, "Carbon sequestration-oriented forest management plans," in *Proc. IEEE 6th Inf. Technol. Autom. Control Conf.*, 2023, pp. 1396–1400, doi: 10.1109/ITNEC56291.2023.10082340.

[2] D. Schimel et al., "Observing terrestrial ecosystems and the carbon cycle from space," *Glob. Change Biol.*, vol. 21, no. 5, pp. 1762–1776, May 2015, doi: 10.1111/GCB.12822.

[3] Y. Malhi, P. Meir, and S. Brown, "Forests, carbon and global climate," *Philos. Trans. R. Soc. London. Ser. A Math. Phys. Eng. Sci.*, vol. 360, no. 1797, pp. 1567–1591, Aug. 2002, doi: 10.1098/RSTA.2002.1020.

[4] A. Olesk, J. Praks, O. Antropov, K. Zalite, T. Arumäe, and K. Voormansik, "Interferometric SAR coherence models for characterization of Hemiboreal forests using TanDEM-X data," *Remote Sens.*, vol. 8, no. 9, p. 700, Aug. 2016, doi: 10.3390/RS8090700.

[5] Z. Xi, H. Xu, Y. Xing, W. Gong, G. Chen, and S. Yang, "Forest canopy height mapping by synergizing ICESat-2, Sentinel-1, Sentinel-2 and topographic information based on machine learning methods," *Remote Sens.*, vol. 14, no. 2, p. 364, Jan. 2022, doi: 10.3390/RS14020364.

[6] J. Praks, O. Antropov, A. Olesk, and K. Voormansik, "Forest height estimation from TanDEM-X images with semi-empirical coherence models," in *Proc. Int. Geosci. Remote Sens. Symp.*, 2018, pp. 8805–8808, doi: 10.1109/IGARSS.2018.8519569.

[7] M. Namiranian, *Measurement of the Tree and Forest Biometry*. Tehran, Iran: Univ. Tehran Press, 2006.

[8] R. Treuhaft et al., "Tropical-forest structure and biomass dynamics from TanDEM-X radar interferometry," *Forests*, vol. 8, no. 8, Jul. 2017, Art. no. 277, doi: 10.3390/F8080277.

[9] S. Roy et al., "Estimating above ground biomass (AGB) and tree density using sentinel-1 data," *Environ. Sci. Eng.*, pp. 259–280, 2021, doi: 10.1007/978-3-030-56542-8_11/COVER.

[10] D. Timothy, M. Onisimo, and I. Riyad, "Quantifying aboveground biomass in African environments: A review of the trade-offs between sensor estimation accuracy and costs," *Trop. Ecol.*, vol. 57, no. 3, pp. 393–405, 2016.

[11] R. Valbuena et al., "Enhancing of accuracy assessment for forest aboveground biomass estimates obtained from remote sensing via hypothesis testing and overfitting evaluation," *Ecol. Model.*, vol. 366, pp. 15–26, Dec. 2017, doi: 10.1016/J.ECOLMODEL.2017.10.009.

[12] P. Rodríguez-Veiga, J. Wheeler, V. Louis, K. Tansey, and H. Balzter, "Quantifying forest biomass carbon stocks from space," *Curr. Forestry Rep.*, vol. 3, no. 1, pp. 1–18, Mar. 2017, doi: 10.1007/S40725-017-0052-5/FIGURES/4.

[13] D. Lu, Q. Chen, G. Wang, L. Liu, G. Li, and E. Moran, "A survey of remote sensing-based aboveground biomass estimation methods in forest ecosystems," *Int. J. Digit. Earth*, vol. 9, no. 1, pp. 63–105, 2016, doi: 10.1080/17538947.2014.990526.

[14] C. Singh, S. K. Karan, P. Sardar, and S. R. Samadder, "Remote sensing-based biomass estimation of dry deciduous tropical forest using machine learning and ensemble analysis," *J. Environ. Manage.*, vol. 308, Apr. 2022, Art. no. 114639, doi: 10.1016/J.JENVMAN.2022.114639.

[15] S. Sinha, C. Jeganathan, L. K. Sharma, and M. S. Nathawat, "A review of radar remote sensing for biomass estimation," *Int. J. Environ. Sci. Technol.*, vol. 12, no. 5, pp. 1779–1792, May 2015, doi: 10.1007/S13762-015-0750-0/FIGURES/1.

[16] T. Le Toan, S. Quegan, I. Woodward, M. Lomas, N. Delbart, and G. Picard, "Relating radar remote sensing of biomass to modelling of forest carbon budgets," *Clim. Change*, vol. 67, no. 2/3, pp. 379–402, Dec. 2004, doi: 10.1007/S10584-004-3155-5/METRICS.

[17] R. B. Thapa, M. Watanabe, T. Motohka, and M. Shimada, "Potential of high-resolution ALOS–PALSAR mosaic texture for aboveground forest carbon tracking in tropical region," *Remote Sens. Environ.*, vol. 160, pp. 122–133, Apr. 2015, doi: 10.1016/J.RSE.2015.01.007.

[18] W. Li, Z. Niu, R. Shang, Y. Qin, L. Wang, and H. Chen, "High-resolution mapping of forest canopy height using machine learning by coupling ICESat-2 LiDAR with Sentinel-1, Sentinel-2 and Landsat-8 data," *Int. J. Appl. Earth Observ. Geoinf.*, vol. 92, Oct. 2020, Art. no. 102163, doi: 10.1016/J.JAG.2020.102163.

[19] L. Li et al., "Reduction in uncertainty in forest aboveground biomass estimation using Sentinel-2 images: A case study of Pinus Densata forests in Shangri-La City, China," *Remote Sens.*, vol. 15, no. 3, p. 559, Jan. 2023, doi: 10.3390/RS15030559.

[20] D. Morin et al., "Estimation and mapping of forest structure parameters from open access satellite images: Development of a generic method with a study case on coniferous plantation," *Remote Sens.*, vol. 11, no. 11, May 2019, Art. no. 1275, doi: 10.3390/RS11111275.

[21] F. Moradi, A. A. Darvishsefat, M. Namiranina, and G. Ronoud, "Investigating the capability of Landsat 8 OLI data for estimation of aboveground woody biomass of common hornbeam (Carpinus Betulus L.) stands in Khyroud forest," *Iranian J. Forest Poplar Res.*, vol. 26, no. 3, pp. 406–420, 2018.

[22] S. Pandit, S. Tsuyuki, and T. Dube, "Estimating above-ground biomass in sub-tropical buffer zone community forests, Nepal, using Sentinel 2 data," *Remote Sens.*, vol. 10, no. 4, Apr. 2018, Art. no. 601, doi: 10.3390/RS10040601.

[23] J. A. A. Castillo, A. A. Apan, T. N. Maraseni, and S. G. Salmo, "Estimation and mapping of above-ground biomass of mangrove forests and their replacement land uses in the Philippines using sentinel imagery," *ISPRS J. Photogrammetry Remote Sens.*, vol. 134, pp. 70–85, Dec. 2017, doi: 10.1016/J.ISPRSJPRS.2017.10.016.

[24] G. M. Foody, D. S. Boyd, and M. E. J. Cutler, "Predictive relations of tropical forest biomass from Landsat TM data and their transferability between regions," *Remote Sens. Environ.*, vol. 85, no. 4, pp. 463–474, Jun. 2003, doi: 10.1016/S0034-4257(03)00039-7.

[25] M. Poorazimy, S. Shataee, R. E. McRoberts, and J. Mohammadi, "Integrating airborne laser scanning data, space-borne radar data and digital aerial imagery to estimate aboveground carbon stock in Hyrcanian forests, Iran," *Remote Sens. Environ.*, vol. 240, Apr. 2020, Art. no. 111669, doi: 10.1016/J.RSE.2020.111669.

[26] O. W. Tsui, N. C. Coops, M. A. Wulder, and P. L. Marshall, "Integrating airborne LiDAR and space-borne radar via multivariate kriging to estimate above-ground biomass," *Remote Sens. Environ.*, vol. 139, pp. 340–352, 2013, doi: 10.1016/j.rse.2013.08.012.

[27] M. Santoro and O. Cartus, "ESA biomass climate change initiative (biomass_cci): Global datasets of forest above-ground biomass for the years 2010, 2017 and 2018, v2," Centre Environ. Data Anal., Didcot, U.K., 2021.

[28] J. I. H. Askne and M. Santoro, "On the estimation of boreal forest biomass from TanDEM-X data without training samples," *IEEE Geosci. Remote Sens. Lett.*, vol. 12, no. 4, pp. 771–775, Apr. 2015, doi: 10.1109/LGRS.2014.2361393.

[29] A. T. Caicoya, F. Kugler, I. Hajnsek, and K. Papathanassiou, "Boreal forest biomass classification with TanDEM-X," in *Proc. IEEE Int. Geosci. Remote Sens. Symp.*, 2012, pp. 3439–3442, doi: 10.1109/IGARSS.2012.6350681.

[30] E. Hansen et al., "Relative efficiency of ALS and InSAR for biomass estimation in a Tanzanian rainforest," *Remote Sens.*, vol. 7, no. 8, pp. 9865–9885, Aug. 2015, doi: 10.3390/rs70809865.

[31] S. Abdullahi, F. Kugler, and H. Pretzsch, "Prediction of stem volume in complex temperate forest stands using TanDEM-X SAR data," *Remote Sens. Environ.*, vol. 174, pp. 197–211, Mar. 2016, doi: 10.1016/j.rse.2015.12.012.

[32] M. Schlund, F. von Poncet, S. Kuntz, C. Schmullius, and D. H. Hoekman, "TanDEM-X data for aboveground biomass retrieval in a tropical peat swamp forest," *Remote Sens. Environ.*, vol. 158, pp. 255–266, Mar. 2015, doi: 10.1016/j.rse.2014.11.016.

[33] S. Solberg, R. Astrup, J. Breidenbach, B. Nilsen, and D. Weydahl, "Monitoring spruce volume and biomass with InSAR data from TanDEM-X," *Remote Sens. Environ.*, vol. 139, pp. 60–67, Dec. 2013, doi: 10.1016/j.rse.2013.07.036.

[34] S. Solberg, R. Astrup, T. Gobakken, E. Næsset, and D. J. Weydahl, "Estimating spruce and pine biomass with interferometric X-band SAR," *Remote Sens. Environ.*, vol. 114, no. 10, pp. 2353–2360, Oct. 2010, doi: 10.1016/J.RSE.2010.05.011.

[35] S.-K. Lee and T. E. Fatoyinbo, "TanDEM-X Pol-InSAR inversion for mangrove canopy height estimation," *IEEE J. Sel. Topics Appl. Earth Observ. Remote Sens.*, vol. 8, no. 7, pp. 3608–3618, Jul. 2015, doi: 10.1109/JSTARS.2015.2431646.

[36] F. Kugler, D. Schulze, I. Hajnsek, H. Pretzsch, and K. P. Papathanassiou, "TanDEM-X Pol-InSAR performance for forest height estimation," *IEEE Trans. Geosci. Remote Sens.*, vol. 52, no. 10, pp. 6404–6422, Oct. 2014, doi: 10.1109/TGRS.2013.2296533.

[37] J. Praks, O. Antropov, and M. T. Hallikainen, "LIDAR-aided SAR interferometry studies in Boreal forest: Scattering phase center and extinction coefficient at X- and L-band," *IEEE Trans. Geosci. Remote Sens.*, vol. 50, no. 10, pp. 3831–3843, Oct. 2012, doi: 10.1109/TGRS.2012.2185803.

[38] I. Hajnsek, F. Kugler, S. K. Lee, and K. P. Papathanassiou, "Tropical-forest-parameter estimation by means of Pol-InSAR: The INDREX-II campaign," *IEEE Trans. Geosci. Remote Sens.*, vol. 47, no. 2, pp. 481–493, Feb. 2009, doi: 10.1109/TGRS.2008.2009437.

[39] S. R. Cloude, H. Chen, and D. G. Goodenough, "Forest height estimation and validation using TanDEM-X polinsar," in *Proc. IEEE Int. Geosci. Remote Sens. Symp.*, 2013, pp. 1889–1892, doi: 10.1109/IGARSS.2013.6723172.

[40] M. Schlund, F. von Poncet, D. H. Hoekman, S. Kuntz, and C. Schmullius, "Importance of bistatic SAR features from TanDEM-X for forest mapping and monitoring," *Remote Sens. Environ.*, vol. 151, pp. 16–26, Aug. 2014, doi: 10.1016/j.rse.2013.08.024.

[41] G. Ronoud, A. A. Darvishsefat, M. E. Schaepman, M. Namiranian, and Y. Maghsoudi, "Woody aboveground biomass estimation using radar data in the mixed Hyrcanian forest (case study: Khayroud forest of Nowshahr, Mazandaran)," *Iranian J. Forest*, vol. 14, no. 3, pp. 257–274, Nov. 2022, doi: 10.22034/IJF.2022.310971.1808.

[42] C. Gomez et al., "Canopy height estimation in Mediterranean forests of Spain with TanDEM-X data," *IEEE J. Sel. Topics Appl. Earth Observ. Remote Sens.*, vol. 14, pp. 2956–2970, 2021, doi: 10.1109/JSTARS.2021.3060691.

[43] S. Solberg, J. May, W. Bogren, J. Breidenbach, T. Torp, and B. Gizachew, "Interferometric SAR DEMs for forest change in Uganda 2000–2012," *Remote Sens.*, vol. 10, no. 2, Feb. 2018, Art. no. 228, doi: 10.3390/rs10020228.

[44] M. Schlund and H.-D. V. Boehm, "Assessment of linear relationships between TanDEM-X coherence and canopy height as well as aboveground biomass in tropical forests," *Int. J. Remote Sens.*, vol. 42, no. 9, pp. 3405–3425, May 2021, doi: 10.1080/01431161.2020.1871101.

[45] H. Chen, S. R. Cloude, and D. G. Goodenough, "Forest canopy height estimation using TanDEM-X coherence data," *IEEE J. Sel. Topics Appl. Earth Observ. Remote Sens.*, vol. 9, no. 7, pp. 3177–3188, Jul. 2016, doi: 10.1109/JSTARS.2016.2582722.

[46] T. Aulinger, T. Mette, K. P. Papathanassiou, I. Hajnsek, M. Heurich, and P. Krzystek, "Validation of heights from interferometric SAR and LiDAR over the temperate forest site 'Nationalpark Bayerischer Wald,'" *Eur. Space Agency*, no. 586, pp. 67–72, 2005.

[47] S. Erasmi, M. Semmler, P. Schall, and M. Schlund, "Sensitivity of bistatic TanDEM-X data to stand structural parameters in temperate forests," *Remote Sens.*, vol. 11, no. 24, Dec. 2019, Art. no. 2966, doi: 10.3390/RS11242966.

[48] T. Nakai, A. Sumida, Y. Kodama, T. Hara, and T. Ohta, "A comparison between various definitions of forest stand height and aerodynamic canopy height," *Agricultural Forest Meteorol.*, vol. 150, no. 9, pp. 1225–1233, Aug. 2010, doi: 10.1016/J.AGRFORMET.2010.05.005.

[49] S. Brown, A. J. R. Gillespie, and A. E. Lugo, "Biomass estimation methods for tropical forests with applications to forest inventory data," *Forest Sci.*, vol. 35, no. 4, pp. 881–902, Dec. 1989, doi: 10.1093/FORESTSCIENCE/35.4.881.

[50] Faculty members of Forestry and Forest Economics Department, "Gorazbon district revision forestry project, experimental and research forest Tehran University (Kheyrud forest)," Tehran University, Karaj, Iran, 2010.

[51] A. A. Enayati, *Wood Physics*. Tehran, Iran: Univ. Tehran Press, 2011.

[52] S. Brown and A. E. Lugo, "Biomass of tropical forests: A new estimate based on forest volumes," *Science*, vol. 223, no. 4642, pp. 1290–1293, Mar. 1984, doi: 10.1126/SCIENCE.223.4642.1290.

[53] A. Tarmian, R. Remond, M. Faezipour, A. Karimi, and P. Perré, "Reaction wood drying kinetics: Tension wood in Fagus Sylvatica and compression wood in Picea Abies," *Wood Sci. Technol.*, vol. 43, no. 1/2, pp. 113–130, Feb. 2009, doi: 10.1007/s00226-008-0230-5.

[54] S. R. Cloude and K. P. Papathanassiou, "Polarimetric optimisation in radar interferometry," *Electron. Lett.*, vol. 33, no. 13, pp. 1176–1178, 1997, doi: 10.1049/el:19970790.

[55] D. Small and A. Schubert, "Guide to ASAR geocoding guide to ASAR geocoding," *Univ. Zurich*, no. 1, vol. 1, pp. 1–36, 2008.

[56] S. R. Cloude and K. P. Papathanassiou, "Three-stage inversion process for polarimetric SAR interferometry," *IEE Proc. Radar, Sonar Navigation*, vol. 150, no. 3, pp. 125–134, 2003, doi: 10.1049/ip-rsn:20030449.

[57] A. Olesk, K. Voormansik, A. Vain, M. Noorma, and J. Praks, "Seasonal differences in forest height estimation from interferometric TanDEM-X coherence data," *IEEE J. Sel. Topics Appl. Earth Observ. Remote Sens.*, vol. 8, no. 12, pp. 5565–5572, Dec. 2015, doi: 10.1109/JSTARS.2015.2501648.

[58] J. S. Lee, "Refined filtering of image noise using local statistics," *Comput. Graph. Image Process.*, vol. 15, no. 4, pp. 380–389, Apr. 1981, doi: 10.1016/S0146-664X(81)80018-4.

[59] Y. Liu, W. Gong, Y. Xing, X. Hu, and J. Gong, "Estimation of the forest stand mean height and aboveground biomass in Northeast China using SAR Sentinel-1B, multispectral Sentinel-2A, and DEM imagery," *ISPRS J. Photogrammetry Remote Sens.*, vol. 151, pp. 277–289, May 2019, doi: 10.1016/J.ISPRSJPRS.2019.03.016.

[60] L. Chen, C. Ren, B. Zhang, Z. Wang, and Y. Xi, "Estimation of forest above-ground biomass by geographically weighted regression and machine learning with sentinel imagery," *Forests*, vol. 9, no. 10, p. 582, Sep. 2018, doi: 10.3390/F9100582.

[61] J. Louis et al., "Sentinel-2 SEN2COR: L2A processor for users," in *European Space Agency, (Special Publication) ESA SP*, vol. SP-740, 2016.

[62] M. Drusch et al., "Sentinel-2: ESA's optical high-resolution mission for GMES operational services," *Remote Sens. Environ.*, vol. 120, pp. 25–36, May 2012, doi: 10.1016/j.rse.2011.11.026.

[63] B. Putzenlechner et al., "Validation of Sentinel-2 fAPAR products using ground observations across three forest ecosystems," *Remote Sens. Environ.*, vol. 232, Oct. 2019, Art. no. 111310, doi: 10.1016/j.rse.2019.111310.

[64] M. Weiss and F. Baret, "S2ToolBox Level 2 products: LAI, FAPAR, FCOVER–Version 1.1," *Sentin. ToolBox Level2 Prod.*, 2016.

[65] S. Jacquemoud et al., "PROSPECT + SAIL models: A review of use for vegetation characterization," *Remote Sens. Environ.*, vol. 113, no. 1, pp. S56–S66, Sep. 2009, doi: 10.1016/J.RSE.2008.01.026.

[66] C. J. Tucker, "Red and photographic infrared linear combinations for monitoring vegetation," *Remote Sens. Environ.*, vol. 8, no. 2, pp. 127–150, May 1979, doi: 10.1016/0034-4257(79)90013-0.

[67] J.-L. Roujean and F.-M. Breon, "Estimating PAR absorbed by vegetation from bidirectional reflectance measurements," *Remote Sens. Environ.*, vol. 51, no. 3, pp. 375–384, Mar. 1995, doi: 10.1016/0034-4257(94)00114-3.

[68] C. Buschmann and E. Nagel, "In vivo spectroscopy and internal optics of leaves as basis for remote sensing of vegetation," *Int. J. Remote Sens.*, vol. 14, no. 4, pp. 711–722, Mar. 1993, doi: 10.1080/01431169308904370.

[69] R. CRIPPEN, "Calculating the vegetation index faster," *Remote Sens. Environ.*, vol. 34, no. 1, pp. 71–73, Oct. 1990, doi: 10.1016/0034-4257(90)90085-Z.

[70] C. F. Jordan, "Derivation of leaf-area index from quality of light on the forest floor," *Ecology*, vol. 50, no. 4, pp. 663–666, Jul. 1969, doi: 10.2307/1936256.

[71] B. Pinty and M. M. Verstraete, "GEMI: A non-linear index to monitor global vegetation from satellites," *Vegetatio*, vol. 101, no. 1, pp. 15–20, 1992, doi: 10.1007/BF00031911.

[72] J. Dash and P. J. Curran, "The MERIS terrestrial chlorophyll index," *Int. J. Remote Sens.*, vol. 25, no. 23, pp. 5403–5413, 2004, doi: 10.1080/0143116042000274015.

[73] G. Guyot, F. Baret, and S. Jacquemoud, *Imaging Spectroscopy for Vegetation Studies*, vol. 2. Norwell, MA, USA: Kluwer, 1992.

[74] J. Delegido, J. Verrelst, L. Alonso, and J. Moreno, "Evaluation of Sentinel-2 red-edge bands for empirical estimation of green LAI and chlorophyll content," *Sensors*, vol. 11, no. 7, pp. 7063–7081, Jul. 2011, doi: 10.3390/s110707063.

[75] G. A. Blackburn, "Spectral indices for estimating photosynthetic pigment concentrations: A test using senescent tree leaves," *Int. J. Remote Sens.*, vol. 19, no. 4, pp. 657–675, Jan. 1998, doi: 10.1080/014311698215919.

[76] G. Guyot and F. Baret, "Utilisation de la haute resolution spectrale pour suivre l'etat des couverts vegetaux," *Spectral Signatures Objects Remote Sens.*, vol. 287, pp. 279–286, 1988.

[77] M. Kuhn, "Package 'caret'–Classification and regression training," *CRAN Repository*, 2019.

[78] H. J. Persson, J. Jonzén, and M. Nilsson, "Combining TanDEM-X and Sentinel-2 for large-area species-wise prediction of forest biomass and volume," *Int. J. Appl. Earth Observ. Geoinformation*, vol. 96, Apr. 2021, Art. no. 102275, doi: 10.1016/j.jag.2020.102275.

[79] E. Tomppo and M. Halme, "Using coarse scale forest variables as ancillary information and weighting of variables in k-NN estimation: A genetic algorithm approach," *Remote Sens. Environ.*, vol. 92, no. 1, pp. 1–20, Jul. 2004, doi: 10.1016/J.RSE.2004.04.003.

[80] E. Tomppo, H. Olsson, G. Ståhl, M. Nilsson, O. Hagner, and M. Katila, "Combining national forest inventory field plots and remote sensing data for forest databases," *Remote Sens. Environ.*, vol. 112, no. 5, pp. 1982–1999, May 2008, doi: 10.1016/J.RSE.2007.03.032.

[81] S. Antonova et al., "Estimating tree height from TanDEM-X data at the Northwestern Canadian treeline," *Remote Sens. Environ.*, vol. 231, Sep. 2019, Art. no. 111251, doi: 10.1016/J.RSE.2019.111251.

[82] M. A. Tanase, R. Panciera, K. Lowell, S. Tian, J. M. Hacker, and J. P. Walker, "Airborne multi-temporal L-band polarimetric SAR data for biomass estimation in semi-arid forests," *Remote Sens. Environ.*, vol. 145, pp. 93–104, Apr. 2014, doi: 10.1016/J.RSE.2014.01.024.

[83] L. Breiman, "Random forests," *Mach. Learn.*, vol. 45, no. 1, pp. 5–32, 2001.

[84] C. Cortes, V. Vapnik, and L. Saitta, "Support-vector networks," *Mach. Learn.*, vol. 20, no. 3, pp. 273–297, Sep. 1995, doi: 10.1007/BF00994018.

[85] L. C. Wensel, W. J. Meerschaert, and G. S. Biging, "Tree height and diameter growth models for Northern California conifers," *Hilgardia*, vol. 55, no. 8, pp. 1–20, Oct. 1987, doi: 10.3733/hilg.v55n08p020.

[86] J. A. Johannessen and F. Collard, "SAR instrument principles and processing," in *Proc. 3rd ESA Adv. Training Ocean Remote Sens.*, 2013, pp. 1–40.

[87] G. V. Laurin et al., "Optical and SAR sensor synergies for forest and land cover mapping in a tropical site in West Africa," *Int. J. Appl. Earth Observ. Geoinformation*, vol. 21, pp. 7–16, Apr. 2013, doi: 10.1016/j.jag.2012.08.002.

[88] S. M. Ghosh, M. D. Behera, and S. Paramanik, "Canopy height estimation using sentinel series images through machine learning models in a Mangrove forest," *Remote Sens.*, vol. 12, no. 9, May 2020, Art. no. 1519, doi: 10.3390/rs12091519.

[89] P. M. López-Serrano, C. A. López-Sánchez, J. G. Álvarez-González, and J. García-Gutiérrez, "A comparison of machine learning techniques applied to Landsat-5 TM spectral data for biomass estimation," *Can. J. Remote Sens.*, vol. 42, no. 6, pp. 690–705, Nov. 2016, doi: 10.1080/07038992.2016.1217485.

[90] M. L. Imhoff, "Radar backscatter and biomass saturation: Ramifications for global biomass inventory," *IEEE Trans. Geosci. Remote Sens.*, vol. 33, no. 2, pp. 511–518, Mar. 1995, doi: 10.1109/TGRS.1995.8746034.

[91] M. Pourshamsi et al., "Tropical forest canopy height estimation from combined polarimetric SAR and LiDAR using machine-learning," *ISPRS J. Photogrammetry Remote Sens.*, vol. 172, pp. 79–94, Feb. 2021, doi: 10.1016/j.isprsjprs.2020.11.008.

[92] J. A. Navarro, N. Algeet, A. Fernández-Landa, J. Esteban, P. Rodríguez-Noriega, and M. L. Guillén-Climent, "Integration of UAV, Sentinel-1, and Sentinel-2 data for mangrove plantation aboveground biomass monitoring in Senegal," *Remote Sens.*, vol. 11, no. 1, Jan. 2019, Art. no. 77, doi: 10.3390/rs11010077.

[93] M. R. Pourrahmati et al., "Mapping Lorey's height over Hyrcanian forests of Iran using synergy of ICESat/GLAS and optical images," *Eur. J. Remote Sens.*, vol. 51, no. 1, pp. 100–115, Jan. 2018, doi: 10.1080/22797254.2017.1405717.

[94] M. C. Dobson, F. T. Ulaby, T. LeToan, A. Beaudoin, E. S. Kasischke, and N. Christensen, "Dependence of radar backscatter on coniferous forest biomass," *IEEE Trans. Geosci. Remote Sens.*, vol. 30, no. 2, pp. 412–415, Mar. 1992, doi: 10.1109/36.134090.

[95] E. M. O. Silveira et al., "Nationwide native forest structure maps for Argentina based on forest inventory data, SAR Sentinel-1 and vegetation metrics from Sentinel-2 imagery," *Remote Sens. Environ.*, vol. 285, Feb. 2023, Art. no. 113391, doi: 10.1016/j.rse.2022.113391.

[96] R. M. David, N. J. Rosser, and D. N. M. Donoghue, "Improving above ground biomass estimates of Southern Africa dryland forests by combining Sentinel-1 SAR and Sentinel-2 multispectral imagery," *Remote Sens. Environ.*, vol. 282, Dec. 2022, Art. no. 113232, doi: 10.1016/j.rse.2022.113232.

[97] M. Van Pham et al., "Integrating Sentinel-1A SAR data and GIS to estimate aboveground biomass and carbon accumulation for tropical forest types in Thuan Chau district, Vietnam," *Remote Sens. Appl. Soc. Environ.*, vol. 14, pp. 148–157, Apr. 2019, doi: 10.1016/j.rsase.2019.03.003.

[98] O. Antropov, Y. Rauste, T. Hame, and J. Praks, "Combining TanDEM-X and Landsat 8 data for improved mapping of forest biomass," in *Proc. IEEE Int. Geosci. Remote Sens. Symp.*, 2015, pp. 3862–3865, doi: 10.1109/IGARSS.2015.7326667.

[99] S. Nandy, R. Srinet, and H. Padalia, "Mapping forest height and aboveground biomass by integrating ICESat-2, Sentinel-1 and Sentinel-2 data using random forest algorithm in Northwest Himalayan foothills of India," *Geophys. Res. Lett.*, vol. 48, no. 14, Jul. 2021, Art. no. e2021GL093799, doi: 10.1029/2021GL093799.

[100] M. Schlund, F. von Poncet, S. Kuntz, H.-D. V. Boehm, D. H. Hoekman, and C. Schmullius, "TanDEM-X elevation model data for canopy height and aboveground biomass retrieval in a tropical peat swamp forest," *Int. J. Remote Sens.*, vol. 37, no. 21, pp. 5021–5044, Nov. 2016, doi: 10.1080/01431161.2016.1226001.

[101] A. T. Caicoya, F. Kugler, I. Hajnsek, and K. P. Papathanassiou, "Large-scale biomass classification in Boreal forests with TanDEM-X Data," *IEEE Trans. Geosci. Remote Sens.*, vol. 54, no. 10, pp. 5935–5951, Oct. 2016, doi: 10.1109/TGRS.2016.2575542.

[102] S. Vafaei et al., "Improving accuracy estimation of forest aboveground biomass based on incorporation of ALOS-2 PALSAR-2 and Sentinel-2A imagery and machine learning: A case study of the Hyrcanian forest area (Iran)," *Remote Sens.*, vol. 10, no. 2, Jan. 2018, Art. no. 172, doi: 10.3390/rs10020172.

[103] L. Chen et al., "Improved object-based estimation of forest aboveground biomass by integrating LiDAR Data from GEDI and ICESat-2 with multi-sensor images in a heterogeneous mountainous region," *Remote Sens.*, vol. 14, no. 12, Jun. 2022, Art. no. 2743, doi: 10.3390/rs14122743.

[104] C. Li, L. Zhou, and W. Xu, "Estimating aboveground biomass using Sentinel-2 MSI data and ensemble algorithms for grassland in the Shengjin Lake Wetland, China," *Remote Sens.*, vol. 13, no. 8, Apr. 2021, Art. no. 1595, doi: 10.3390/rs13081595.

[105] R. Bhattarai, P. Rahimzadeh-Bajgiran, A. Weiskittel, S. Homayouni, T. W. Gara, and R. P. Hanavan, "Estimating species-specific leaf area index and basal area using optical and SAR remote sensing data in Acadian mixed spruce-fir forests, USA," *Int. J. Appl. Earth Observ. Geoinformation*, vol. 108, Apr. 2022, Art. no. 102727, doi: 10.1016/j.jag.2022.102727.

[106] P. T. Wolter and P. A. Townsend, "Multi-sensor data fusion for estimating forest species composition and abundance in northern Minnesota," *Remote Sens. Environ.*, vol. 115, no. 2, pp. 671–691, Feb. 2011, doi: 10.1016/j.rse.2010.10.010.

[107] G. Ronoud, P. Fatehi, A. A. Darvishsefat, E. Tomppo, J. Praks, and M. E. Schaepman, "Multi-sensor aboveground biomass estimation in the broadleaved Hyrcanian forest of Iran," *Can. J. Remote Sens.*, vol. 47, no. 6, pp. 818–834, 2021, doi: 10.1080/07038992.2021.1968811.

[108] S. Attarchi and R. Gloaguen, "Improving the estimation of above ground biomass using dual polarimetric PALSAR and ETM+ data in the Hyrcanian Mountain forest (Iran)," *Remote Sens.*, vol. 6, no. 5, pp. 3693–3715, Apr. 2014, doi: 10.3390/rs6053693.

[109] M. G. Motlagh, S. B. Kafaky, A. Mataji, and R. Akhavan, "Estimating and mapping forest biomass using regression models and spot-6 images (case study: Hyrcanian forests of North of Iran)," *Environ. Monit. Assessment*, vol. 190, no. 6, Jun. 2018, Art. no. 352, doi: 10.1007/s10661-018-6725-0.